ELSEVIER

Ultramicroscopy 72 (1998) 109–119

ultramicroscopy

Residual wave aberrations in the first spherical aberration corrected transmission electron microscope

Stephan Uhlemann*,[1], Maximilian Haider[1]

EMBL Heidelberg, PF 102209, D-69012 Heidelberg, Germany

Received 5 May 1997; received in revised form 2 October 1997

Abstract

Here we demonstrate the optical properties of a spherical aberration corrected transmission electron microscope by means of beam tilt series. The high-resolution capabilities are characterized by the measured residual wave aberrations up to the fifth order. Limits for the wave aberration coefficients are determined. We compare the phase-contrast transfer function of the corrected versus the uncorrected objective lens with the help of diffractograms. The information limit and the improvement of the point resolution is discussed.

1. Introduction

For the characterization of novel materials such as ceramics, metal alloys, semiconductor systems, and high-T_c superconductors at an atomic level one needs to have images with an interpretable resolution down to 1 Å. The high interest in such images was the reason to start projects as large as the Brite–Euram project at the beginning of the 1990s [1], to install a 1.2 MeV transmission electron microscope (TEM) in Stuttgart in 1992 [2], and to start in 1992 with the development of a corrected TEM at the EMBL in Heidelberg [3].

Up to now, the application of a transmission electron microscope in order to obtain high-resolution information involves the problem of objective lens aberrations. Those parts of the object wave which carry the most interesting information pass the outer zones of the objective lens and suffer from large additional phase shifts. If the microscope is aligned properly, the wave aberrations are mainly caused by the spherical aberration (C_s) of the objective lens. Scherzer has proven in 1936, that the spherical aberration cannot be avoided in rotational symmetric electro magnetic fields (Scherzer theorem) [4]. In the state-of-the-art transmission electron microscopes the spherical aberration has been optimized in some sense, often at the expense of working distance. However, the optical properties of the objective lens are far away from the ideal case.

Exactly 50 years ago, Scherzer proposed a hardware corrector for the spherical and the chromatic aberration consisting of multipole lenses. The elimination of the aberrations is possible since the

* Corresponding author.

[1] Present adress: CEOS GmbH, Im Neuenheimer Feld 519, D-69120 Heidelberg, Germany.

0304-3991/98/$19.00
PII S0304-3991(97)00102-2

theorem does not apply in this case. Due to technical difficulties, several attempts to improve the optical performance of a TEM according to these suggestions failed [5]. In our project we have built a corrector which was described by Rose [6]. This system can only compensate for the spherical aberration and provides nearly aplanatic imaging conditions. On the other hand, it implies less technical problems. Leaving the chromatic aberration uncorrected can be accepted, if we consider only microscopes which provide a sufficient information limit and if we neglect the contrast contribution of inelastically scattered electrons. We have integrated the corrector in a standard 200 kV Philips CM200ST microscope which is equipped with a field emission gun.

Having the spherical aberration corrected, one recognizes many advantages. First of all, and most obvious in terms of ray optics: The elastically scattered beams emanating from one object point no longer produce a relatively large intensity disk of several nanometers in the final image, often referred to as point spread. The (minimum) diameter of this disk and thus the delocalization of the object information [7] is strongly reduced (proportional to C_s!). This effect is the first visible benefit of the C_s correction. At the right defocus the delocalization can be reduced (at least theoretically) to values even smaller than 1 Å. Thus, the interference patterns in the final image plane produced by different object areas are well separated. As a result, the images of irregularities in a crystalline object such as interfaces or defects can be interpreted more intuitively. The first images which demonstrate this effect will be published in a subsequent paper [8].

Even if the image obtained with the corrected lens contains severe artifacts due to nonlinear contrast mechanisms, the image simulation and the subsequent comparison with experimental images will strongly benefit from the corrected lens. Due to the absence of contrast delocalization it should be much easier to extract an atomic structure model as input for the image simulation.

In terms of wave optics one can state that the information in the recorded intensity pattern is coded in a simpler way, since the corrected lens can supply a phase shift around $\pi/2$ (phase contrast) or around zero (amplitude contrast) for the scattered beams within the whole aperture given by the information limit. This capability directly results in an improved point resolution in the sense of Scherzers definition [9] proportional to $\sqrt[4]{C_s}$. On the other hand, eliminating the phase contrast in the corrected TEM directly is very promising as image simulations reveal [10].

Moreover, small changes in the illumination such as tilt or shift or convergence no longer introduce considerable wave aberrations, which is very advantageous. This means a convergence of the illuminating beam due to the spatial incoherence of the source no longer causes an additional damping of the contrast transfer, provided that the defocus is not too large.

In addition, the correction of the spherical aberration strongly improves the accuracy of the measurement of the residual wave aberrations, as discussed in Section 3. This is mainly due to the fact that one can employ very large illumination tilt angles in the corrected microscope. Therefore, we expect a strong impact of the lens correction in the phase retrieval methods. The focus series reconstruction method and the off-axis holography need to know the phase mask given by the TEM very precisely. This precision can be obtained more conveniently (if at all) in the spherically corrected microscope. Moreover, the guiding principle in holography is to obtain holograms for the minimum gradient of the wave aberration over the whole range of spatial frequencies [11]. These wave aberrations and hence the gradient are strongly reduced in the corrected TEM.

2. Wave aberrations

We describe the transfer function of the microscope T_M in the frame of linear contrast mechanisms by means of standard Fourier optics. Therefore, the effect of the microscope on the object wave Ψ_0 is written in Fourier representation as

$$\Psi_i(g) = \Psi_0(g) T_M = \Psi_0(g) \exp[-i\gamma(g)]. \quad (1)$$

Here Ψ_i represents the Fourier transform of the wave at the image plane. The complex coordinate g is the lattice vector, which is connected with the

Table 1
Wave aberration coefficients and their allowed magnitude calculated from the π/4 limit at 200 kV

Coefficient (symbol)	π/4 limit	π/4 limit at 200 kV for g_{max} =		
		4/nm	7/nm	10/nm
Defocus (C_1, $-\Delta f$)	$\frac{1}{4}(\lambda g_{max}^2)^{-1}$	6.2 nm	− 2.0 nm	1.0 nm
Scherzer focus:		− 69 nm	− 22 nm	− 11 nm
Twofold astigmatism (A_1)	$\frac{1}{4}(\lambda g_{max}^2)^{-1}$	6.2 nm	2.0 nm	1.0 nm
Threefold astigmatism (A_2)	$\frac{3}{8}(\lambda^2 g_{max}^3)^{-1}$	0.93 μm	0.17 μm	60 nm
Axial coma (B_2)	$\frac{1}{8}(\lambda^2 g_{max}^3)^{-1}$	0.31 μm	58 nm	20 nm
Spherical aberration (C_3, C_s)	$\frac{1}{2}(\lambda^3 g_{max}^4)^{-1}$	0.12 mm	13 μm	3.2 μm
Scherzer focus:		1.3 mm	130 μm	32 μm
Fourfold astigmatism (A_3)	$\frac{1}{2}(\lambda^3 g_{max}^4)^{-1}$	0.12 mm	13 μm	3.2 μm
Star aberration (S_3)	$\frac{1}{8}(\lambda^3 g_{max}^4)^{-1}$	31 μm	3.3 μm	0.79 μm
Fivefold astigmatism (A_4)	$\frac{5}{8}(\lambda^4 g_{max}^5)^{-1}$	15 mm	0.94 mm	0.16 mm
Axial coma (B_4)	$\frac{1}{8}(\lambda^4 g_{max}^5)^{-1}$	3.1 mm	0.19 mm	32 μm
Three lobe aberration (D_4)	$\frac{1}{8}(\lambda^4 g_{max}^5)^{-1}$	3.1 mm	0.19 mm	32 μm
Spherical aberration (C_5)	$\frac{3}{4}(\lambda^5 g_{max}^6)^{-1}$	1.8 m	64 mm	7.6 mm
Sixfold astigmatism (A_5)	$\frac{3}{4}(\lambda^5 g_{max}^6)^{-1}$	1.8 m	64 mm	7.6 mm

complex scattering angle ω simply by the relation

$$\omega = \lambda g, \tag{2}$$

if λ is the wavelength of the primary electrons. The function

$$\gamma(g) = 2\pi/\lambda \cdot \chi(\omega) \tag{3}$$

is a real function, because of the conservation of the phase-space volume. Using a common notation, the power series of χ in terms of $\omega = \lambda g$ and its complex conjugate $\bar{\omega}$ can be written as

$$\begin{aligned}\chi(\omega) = \mathrm{Re}\{&\tfrac{1}{2}\omega\bar{\omega}C_1 + \tfrac{1}{2}\bar{\omega}^2A_1 + \omega^2\bar{\omega}B_2 + \tfrac{1}{3}\bar{\omega}^3A_2 \\ &+ \tfrac{1}{4}(\omega\bar{\omega})^2C_3 + \omega^3\bar{\omega}S_3 + \tfrac{1}{4}\bar{\omega}^4A_3 + \omega^3\bar{\omega}^2B_4 \\ &+ \omega^4\bar{\omega}D_4 + \tfrac{1}{5}\bar{\omega}^5A_4 + \tfrac{1}{6}(\omega\bar{\omega})^3C_5 \\ &+ \tfrac{1}{6}\bar{\omega}^6A_5 + \cdots\}.\end{aligned} \tag{4}$$

Considering very old conventions, the index of each coefficient is the order of the corresponding ray aberration, and not of the wave aberration. Thus, for example, the third-order spherical aberration C_s is addressed as C_3. The fractional factor of each term is chosen in such a way that the ray aberration in the image

$$\Delta w_i = 2M\partial_{\bar{\omega}}\chi(\omega) \tag{5}$$

adopts its simplest form. Here M denotes the total magnification of the microscope.

The reasons why we have to include all those strange aberration coefficients listed in Table 1, are twofold: First, most of them could become important at 1 Å resolution, even in the uncorrected microscope. Second, we have measured them in the corrected microscope to make sure that no parasitic aberration limits the point resolution.

In addition, we have listed in Table 1 the allowed magnitude for each coefficient. A maximum parasitic phase shift of π/4 within a given aperture radius g_{max} has been assumed. As we have learned from image simulations, this criterion is a little pessimistic for a single aberration if we consider crystals. On the other hand, cumulative effects caused by different aberrations have been neglected in Table 1.

Since the phase shifts of the rotational symmetric aberrations C_1 and C_3 partly compensate each other[2] if adjusted properly (e.g. Scherzer focus), two values are given. The smaller one, which was calculated from the π/4 limit, can be understood as the necessary stability of the corresponding coefficient. The other (larger) value is calculated for a Scherzer focus which corresponds to the respective g_{max}. The

[2] The constant C_5 of the fifth-order spherical aberration is very small in our corrected TEM (< 10 mm). However, in principle, the phase shift induced by C_5 can also be counterbalanced by C_1 and C_3 in a focus regime with alternating signs.

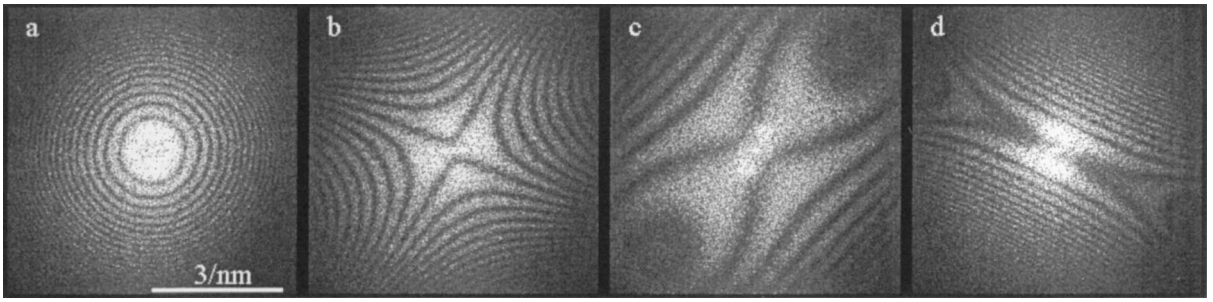

Fig. 1. Typical diffractograms which can be analyzed during the alignment: (a) $C_1 = -633$ nm, $A_1 = 0$; (b) $C_1 = 0$, $A_1 = 308$ nm/$-144°$; (c) $C_1 = 0$, $A_1 = 85$ nm/$-88°$; (d) $C_1 = -404$ nm, $A_1 = 400$ nm/$-53°$. All four diffractograms correspond to the uncorrected state with $C_s = 1290$ μm.

values calculated for C_3 give a hint to what value the spherical aberration of the objective lens needs to be corrected. It turns out that a 10% stability of C_s and Δf is necessary, independent of the point resolution.

This means the absolute accuracy to which C_s must be known is comparable to that which is necessary for the reconstruction methods. Due to the correction of C_s to smaller values, the relative accuracy becomes very uncritical.

3. Measurement of the wave aberrations

For the measurement of the wave aberrations we have chosen the diffractogram tableau method, introduced by Zemlin et al. about 20 years ago [12]. This method has two main advantages. First, it transforms higher-order wave aberrations into first-order aberrations, and second, it does not suffer from object drift problems as do various beam-tilt and cross-correlation (BTXC) methods, which analyze the image shift for a given beam tilt [13,14].

As is known from the theory of linear contrast transfer, only the even part of $\gamma(g)$ can be observed in the Fourier transform of the intensity pattern. This part remains constant under the transformation $g \to -g$, i.e.

$$\gamma_+(g) = \gamma_+(-g) \tag{6}$$

is valid for the even part γ_+. If we assume the object to be amorphous, scattering continuously for all ω in the objective aperture, we can observe the first terms of this even part $\chi_+ = \lambda/(2\pi)\cdot\gamma_+$ of the wave aberration function

$$\chi_+(\omega) = \mathrm{Re}\{\tfrac{1}{2}\omega\bar{\omega}C_1 + \tfrac{1}{2}\bar{\omega}^2A_1 + \tfrac{1}{4}(\omega\bar{\omega})^2C_3 + \omega^3\bar{\omega}S_3 + \tfrac{1}{4}\bar{\omega}^4A_3 + \mathrm{o}(\omega^6)\} \tag{7}$$

provided that the illuminating beam is sufficiently coherent. Since the even part of T_M is represented in the contrast transfer function by a sine function, the intensity I of the Fourier transform of the image of a phase object is proportional to the square

$$I(g) \sim \sin^2[\gamma_+(g)]. \tag{8}$$

If we are not in focus or nearby, the extinction lines of I (zeros of the sine) are determined by C_1 and A_1 and have a more or less elliptic or hyperbolic shape. In the vicinity of $C_1 \approx A_1 \approx 0$ the third-order aberrations can also be observed directly (e.g. Fig. 1c), but not really measured.

As Zemlin et al. suggest [12], we obtain a set (a tableau) of diffractograms, each of which has a different beam tilt. We find for the even part of the wave aberration function of the axis, which is defined by a complex tilt τ of the illuminating beam the expression

$$\chi_+(\omega,\tau) = \tfrac{1}{2}\chi(\omega+\tau) + \tfrac{1}{2}\chi(-\omega+\tau) - \chi(\tau). \tag{9}$$

Now, we identify in $\chi_+(\omega,\tau)$ the quadratic terms proportional to $\omega\bar{\omega}/2$ and $\bar{\omega}^2/4$ with the effective

defocus $C_1(\tau)$ and twofold astigmatism $A_1(\tau)$, respectively. We obtain for the power series in terms of τ and its conjugate $\bar{\tau}$

$$C_1(\tau) = C_1(0) + 4\mathrm{Re}\{\tau B_2\} + 2\tau\bar{\tau}C_3 + 6\mathrm{Re}\{\tau^2 S_3\} + 12\mathrm{Re}\{\tau^2\bar{\tau}B_4\} + 8\mathrm{Re}\{\tau^3 D_4\} + 3(\tau\bar{\tau})^2 C_5 + \cdots \quad (10)$$

and

$$A_1(\tau) = A_1(0) + 2\tau\bar{B}_2 + 2\bar{\tau}A_2 + \tau^2 C_3 + 6\tau\bar{\tau}\bar{S}_3 + 3\bar{\tau}^2 A_3 + 2\tau^3 B_4 + 6\tau^2\bar{\tau}\bar{B}_4 + 12\tau\bar{\tau}^2 D_4 + 4\bar{\tau}^3 A_4 + 2\tau^3\bar{\tau}C_5 + 5\bar{\tau}^4 A_5 + \cdots . \quad (11)$$

Although not explicitly indicated, the aberration coefficients on the right-hand side of Eqs. (10) and (11) are the coefficients of the axis for untilted illumination ($\tau = 0$). If we can determine A_1 and C_1 for a set of different τ, the above two Eqs. (10) and (11) yield an overdetermined system of linear equations for the wanted aberration coefficients, which can be solved by least-square techniques.

The remaining problem is the pattern recognition in order to determine the defocus and the twofold astigmatism of an individual diffractogram. Recently, Thust et al. solved the problem for elliptical diffractograms [15], and applied their solution in a focal-series reconstruction [16]. Within our project, we have developed a different algorithm, which includes also the hyperbolic-shaped diffractograms and even those in between, c.f. cases b–d depicted in Fig. 1. Considering up to 12 zeros (or a phase shift of 12π), our algorithm covers a large range of aberration magnitudes at a given magnification.

We carried out the pattern recognition by means of an external work station in parallel to the collection and Fourier transform of the next CCD image. It takes about 400 ms per diffractogram on a high-end PC. Thus, the time of about 1 min necessary to obtain one tableau is not increased. Moreover, the amount of experimental data necessary for the recognition is reduced. We obtain 16 diffractograms each of which has a size of 256^2 pixel and a depth of 8 bit. This means one tableau is equivalent to one 1024^2 pixel image frame.

4. Residual wave aberrations

4.1. Uncorrected TEM

We start our considerations with a tableau, which was obtained by means of the aligned, but uncorrected microscope. This means the corrector was switched off in this case. The corresponding tableau is depicted in Fig. 2. The central diffraction pattern shows the situation for the untilted beam. We have adjusted a strong underfocus of $\Delta f = -C_1 \approx 590$ nm, nearly free of twofold astigmatism ($|A_1| < 5$ nm). For the determination of C_1 and A_1 we use, in this case, the first eight zeros of the contrast transfer function.

The way the other diffractograms of the tableau are arranged represents the tilt angle and azimuth of the relevant axis. This means the outer 12 diffractograms have the same tilt magnitude (here $|\tau| = 10.8$ mrad), and the azimuth varies in steps of 30°. The remaining three diffractograms have only half of that tilt magnitude ($|\tau| = 5.4$ mrad) and the azimuths 0°, 90°, and 180°, respectively. The meta pixel represents an object area of 1.3×1.3 Å^2 considering the 4×4 binning.

We have aligned the axial coma B_2 by an additional tilt of the illumination which must be considered as an offset of each individual tilt of the tableau. This means the "untilted" central pattern is taken for the so-called coma-free axis. In addition, we have compensated the second-order threefold astigmatism A_2 by means of a sextupole stigmator. For the uncorrected microscope this parasitic aberration is in the order of $|A_2| \approx 1$ μm [16,17].

After these measures have been taken, the resulting tableau in Fig. 2 reflects the rotational symmetry of the spherical aberration. Hence, all diffractograms of the same tilt magnitude show nearly the same magnitudes of twofold astigmatism $|A_1|$ and additional defocus $\Delta C_1 = C_1(\tau) - C_1(0)$. The measured wave aberration coefficients for the illumination axis of the central pattern can be found in Table 2.

A comparison with the values in Table 1 shows that the parasitic aberrations are by far sufficiently small to fulfil the $\pi/4$ limit for an objective aperture of $g_{\max} = 4/\text{nm}$ which contains all reflections necessary to obtain a point resolution of 2.5 Å at the

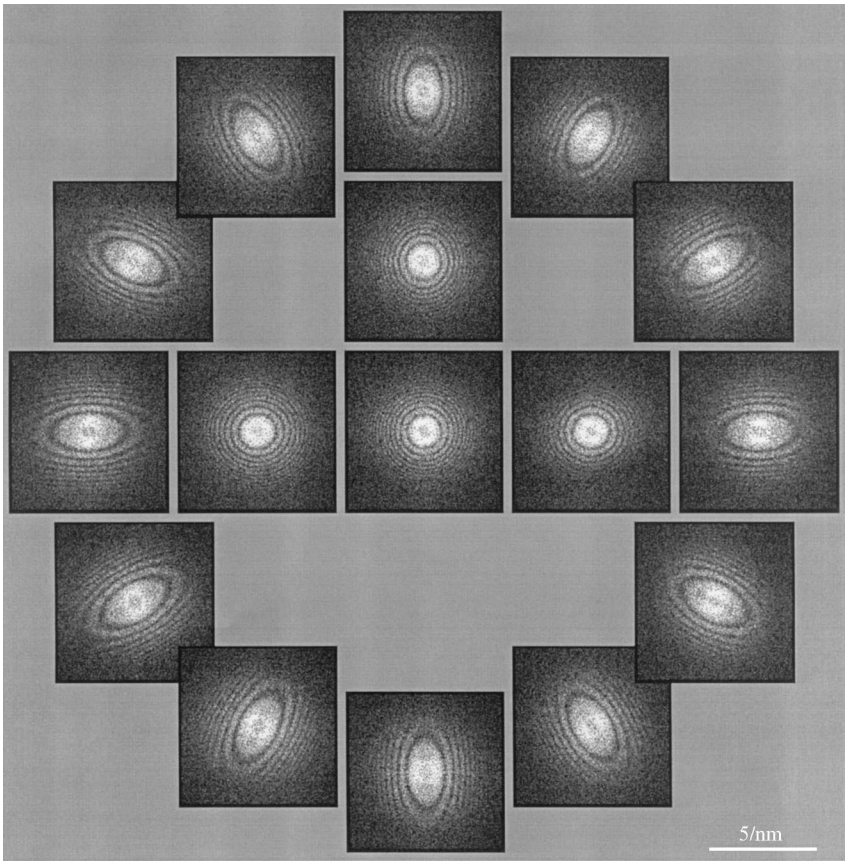

Fig. 2. Tableau obtained by means of the uncorrected, but aligned microscope ($|\tau| = 10.8$ mrad). The position of the diffractograms corresponds to the tilt angle and azimuth. The observed changes in defocus and astigmatism are mainly due to the uncorrected C_s of 1290 μm.

Table 2
Measured wave aberrations for the uncorrected microscope after the alignment

Coefficient	Measured value	Standard deviation
C_1	− 590 nm	10 nm
$\|A_1\|$	0	10 nm
A_2	0.14 μm/120°	0.15 μm
B_2	0.10 μm/80°	0.15 μm
C_3	1290 μm	15 μm

corresponding Scherzer focus of $\Delta f = -C_1 \approx$ 70 nm. The intrinsic higher-order aberrations cannot be measured precisely at this tilt magnitude and are hidden by the dominating C_s. However, as we will see in the following section, they can be neglected for $g_{max} = 4$/nm, since even the parasitic higher-order aberrations measured with the corrector switched on are small compared to the π/4 limits at this small g_{max}.

4.2. Corrected TEM

If we switch the corrector on and go through the alignment procedure, we end up at a corrected C_s with a value of 100 μm, for instance. Here we do not eliminate C_s completely, since we want to keep the possibility of using phase contrast at a new Scherzer focus. Fig. 3 shows the tableau of the corrected TEM taken at the same tilt magnitude of $|\tau| = 10.8$ mrad. Nearly, no effect of the remaining aberrations can be observed at this tilt.

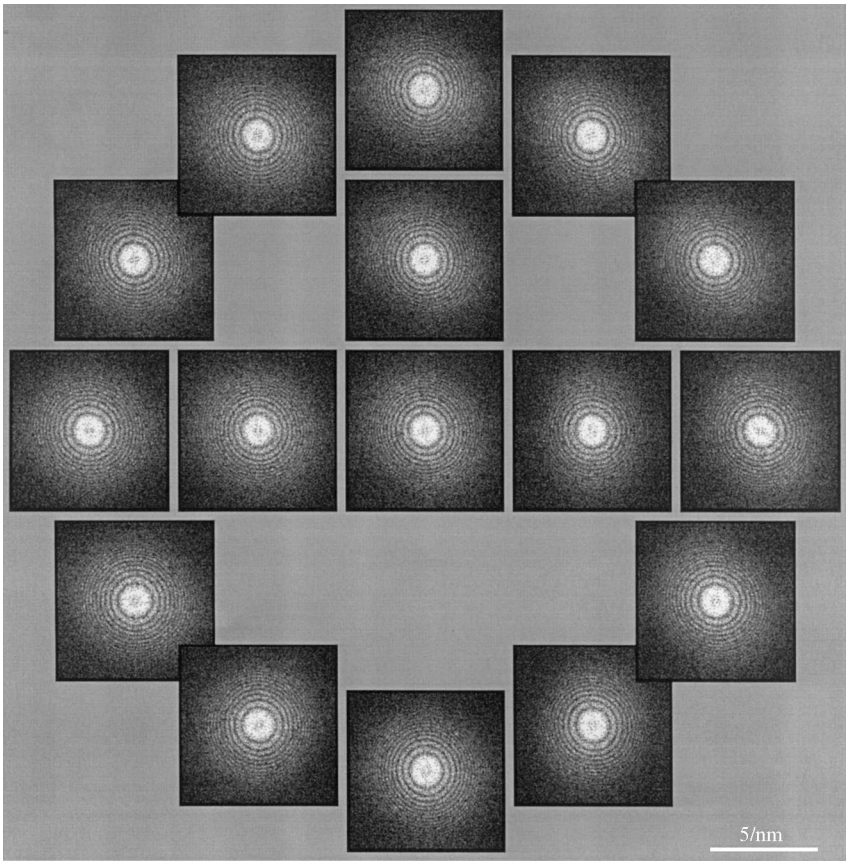

Fig. 3. Tableau obtained by means of the corrected microscope at the same tilt of $|\tau| = 10.8$ mrad. Nearly, no effect of the wave aberrations can be observed at this tilt.

The first impact of the correction of C_s is an increased accuracy of the measured parasitic aberration coefficients. Since C_s no longer introduces that strong twofold astigmatism and defocus when the beam is tilted, we can obtain diffractogram tableaus at very high beam-tilt angles. (In the case of the CM200ST at least up to $|\tau| = 40$ mrad.) The example in Fig. 4 is taken at $|\tau| = 26$ mrad, which is about the scattering angle corresponding to spatial frequencies of 10/nm at 200 kV. The tableau is obtained at the same magnification and defocus $C_1(0)$ as the tableaus before.

Table 3 shows the residual wave aberration coefficients calculated for the tableau in Fig. 4. The given errors represent the standard deviation of the measurement at the given tilt and magnification. For complex coefficients z this standard deviation is calculated as the standard distance

$$\sigma = \sqrt{\frac{1}{N-1}\sum_{n=1}^{N} |z_n - z_{\text{mean}}|^2} \tag{12}$$

of N measurements from the mean z_{mean}. From order to order, the standard deviation of the measured aberrations increase approximately proportional to $1/|\tau_{\text{max}}|$. Therefore, a larger tilt and/or a higher final magnification (which improves the absolute accuracy of the C_1 and A_1 measurements) could further improve the precision of the measured residual wave aberration coefficients. On the other hand, the first-order focusing conditions ($|C_1| \ll 100$ nm and $|A_1| \leqslant 2$ nm) will be adjusted

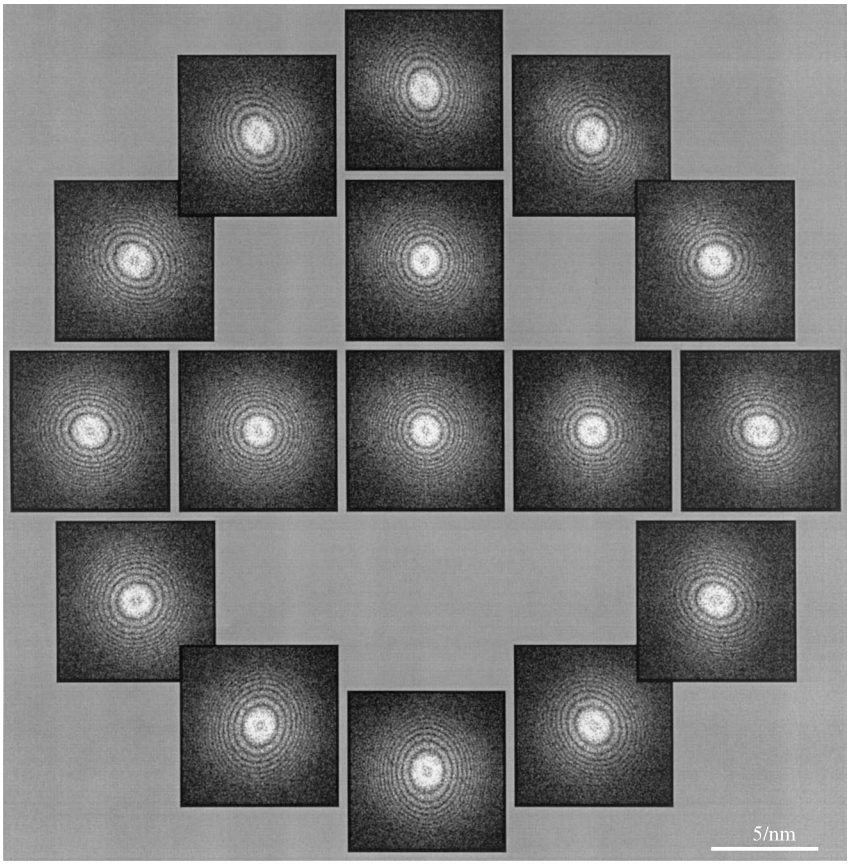

Fig. 4. Tableau obtained with the corrected microscope at a larger tilt of $|\tau| = 26$ mrad. The observed changes in defocus and astigmatism are mainly due to the residual C_s of 90 μm.

Table 3
Wave aberration coefficients of the corrected microscope, measured at a tilt of $|\tau| = 26$ mrad

Coefficient	Measured value	Standard deviation
C_1	− 570 nm	10 nm
A_1	14 nm/146°	10 nm
A_2	250 nm/ − 20°	60 nm
B_2	55 nm/ − 104°	60 nm
C_3	+ 90 μm	3 μm
A_3	5.5 μm/ − 59°	2 μm
S_3	1.6 μm/108°	2 μm
A_4	86 μm/154°	60 μm
B_4	30 μm/ − 141°	30 μm
D_4	19 μm/ − 10°	20 μm
C_5	+ 6 mm	4 mm
A_5	1 mm/150°	2 mm

separately by means of single diffractograms at a higher magnification.

In the example of Fig. 4 the parasitic first-order twofold and the second-order threefold astigmatism violate the π/4 limit. For the experiment described in Section 6, we reduce A_2 further to about $|A_2| < 50$ nm, and eliminate A_1 by means of the objective lens stigmator. Now, all the measured coefficients fulfil the π/4 limit for $g_{max} = 7$/nm, cf. Table 1. Moreover, the measured magnitudes of the fourth-order coefficients (A_4, D_4 and B_4) are comparable to their standard deviation at this tilt angle and final magnification, and are considerably smaller than the π/4 limit for an aperture of 7/nm. This means the power series for the phase shift of the microscope converges rapidly at least within this aperture.

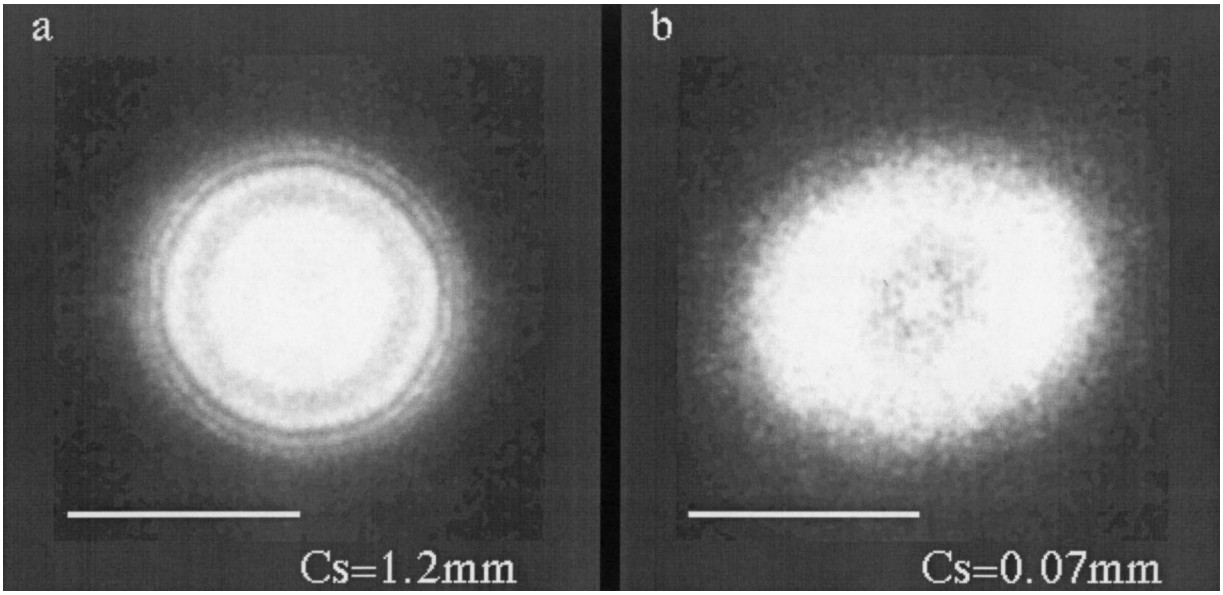

Fig. 5. Illustration of the transfer functions: (a) $C_s = +1230\,\mu m$, $C_1 = -69\,nm$ (Scherzer focus); (b) $C_s = +70\,\mu m$, $C_1 \approx -12\,nm$ (new Scherzer focus). Both diffractograms have the same scale bar corresponding to 7/nm.

5. Information limit and point resolution in the corrected state

One can only make use of the strongly reduced wave aberrations of the microscope if the information transfer from the object to the image is not limited by incoherent damping effects. As mentioned above, our hexapole corrector cannot correct the chromatic aberration of the microscope. Moreover, the necessary transfer lenses of the corrector increase the axial chromatic aberration C_c somewhat, from about 1.3 mm to about 1.7 mm. Unfortunately, this effect causes a stronger damping of the contrast transfer. On the other hand, these shortcomings are counterbalanced by the increased spatial coherence due to the correction of C_s. For small defoci, the latter effect can prevail, especially if we compare a Scherzer focus in the uncorrected TEM and a new Scherzer focus in the corrected TEM.

This comparison can be found in Fig. 5a and b. Both diffractograms are calculated from an image of a amorphous tungsten film (about 2 nm thick) near the respective Scherzer focus. The size of the calibration bars corresponds to a spatial frequency of 7/nm. Fig. 5a shows zeros of the transfer function (the first at 1/2.4 Å), while Fig. 5b does not. The observed intensity of the diffractogram in Fig. 5b is weak in the frequency range $1/1.7 \cdots 1/1.4$ Å and vanishes for larger spatial frequencies. We believe the information limit in the corrected state often to be 1/1.4 Å. This becomes more evident from the Young's fringes diffractogram which can be found in [8].

If we adjust the defocus and the twofold astigmatism carefully by means of online image-and-diffractogram procedures and if we consider the measured second- and higher-order parasitic wave aberrations listed in Table 3, we can state a considerable improvement in the point resolution from 2.4 Å to about 1.4 Å. At present, this point resolution is set by both the information limit and the residual wave aberrations of the corrected microscope.

6. Lifetime of the corrected state

The lifetime of the corrected state is very important for the applicability of the corrected TEM. If

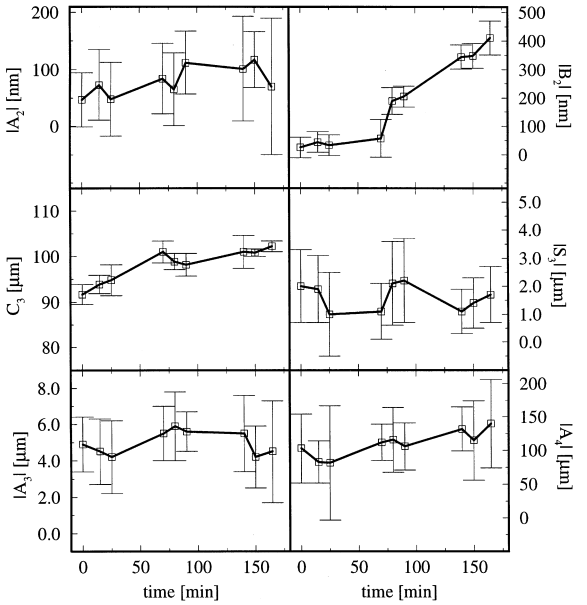

Fig. 6. Development of the residual wave aberrations within 3 h.

the $\pi/4$ limit would be violated a minute after the alignment has been finished, this corrected state would be nearly useless. That is because the user of the microscope has to exchange the amorphous specimen area for an interesting object or object detail. Moreover, it takes the user some time to find the optimum focus or even more to obtain a focus series.

In order to find out whether our microscope can fulfil this demand we have measured the residual aberration coefficients about 50 times within a period of 3 h, and once more 12 h later. We have not switched off the microscope in the meantime. The results of the first 3 h are depicted in Fig. 6. The start time is about the time of the last alignment step, which was the small correction of A_2 mentioned in Section 4.2. The error bars represent the standard deviation (12) of about six averaged measurements from the depicted values of the residual coefficients.

We observed two effects worth mentioning. First, C_s drifted slightly within the first hour of observation. However, this small change in C_s does not really change the point resolution. Second, for some still unknown reasons, the second-order axial coma B_2 jumped suddenly after about 80 min and violated the $\pi/4$ limit. Moreover, in the remaining observation time it drifted at a rate of about 2.5 nm/min. This means the user has to correct for the axial coma from time to time. Fortunately, this can be done at an amorphous edge of the crystal, without exchanging the specimen. All the other coefficients remained constant if we consider their standard deviation. The long-term measurement yielded a similar result. The spherical aberration C_s remained constant. After 12 h we measured for C_s a value of 102 ± 3 µm. For the axial coma which has been corrected after the 3 h of measurement we obtained $|B_2| = 490 \pm 25$ nm at roughly the same azimuth as before. This means that the drift has stopped or continued at a significantly lower drift rate. The measured drift of the defocus and the twofold astigmatism within those 12 h is surprisingly low. We obtained $\Delta C_1 = +90$ nm and $|\Delta A_1| = 30$ nm. All the other parasitic aberrations kept their values within the standard deviation of the measurement.

7. Conclusion and outlook

We have applied the diffractogram-tableau method suggested by Zemlin et al. [12] for the characterization of the spherical-aberration corrected TEM (SACTEM) which was developed in Heidelberg since January 1992. The residual wave aberrations up to the fifth order have been measured, employing large beam-tilt angles of about 26 mrad. After the alignment, the $\pi/4$ limit is fulfilled by every parasitic wave aberration of the corrected microscope within an aperture of at least $g_{max} = 7/\text{nm}$.

As demonstrated by means of diffractogram tableaus, a tilt of the illumination no longer introduces strong wave aberrations. Therefore, the handling of the illuminating beam becomes less critical and the spatial coherence at Scherzer focus is increased. The corrected state of the microscope is quite stable and hence applicable for the user. The semi-automated alignment procedures developed for the corrected TEM are even more convenient than those available for a standard TEM.

At present, the point resolution is limited to about 1.4 Å by both the information limit and the residual wave aberrations of the corrected 200 kV microscope. The delocalization at Scherzer focus can be pushed below this value simply by choosing a sufficiently small C_s. We report on the experiments with Si/CoSi interfaces and the resolution of a GaAs dumbbell structure in a subsequent paper [8].

Acknowledgements

The project was substantially supported by the Volkswagen-Stiftung.

References

[1] D. Van Dyck, H. Lichte, K.D. van der Mast, Ultramicroscopy 64 (1996) 1.
[2] F. Phillip, Ultramicroscopy 56 (1994) 1.
[3] M. Haider, G. Braunshausen, E. Schwan, Optik 99 (1995) 167.
[4] O. Scherzer, Z. Phys. 101 (1936) 593.
[5] H. Hely, Optik 60 (1982) 307, 353.
[6] H. Rose, Optik 85 (1990) 19.
[7] A. Thust, W.M.J. Coene, M. Op de Beeck, D. Van Dyck, Ultramicroscopy 64 (1996) 211.
[8] M. Haider, H. Rose, S. Uhlemann, E. Schwan, B. Kabius, K. Urban, Ultramicroscopy (1997), submitted.
[9] O. Scherzer, J. Appl. Phys. 20 (1949) 20.
[10] M. Foschepoth, H. Kohl, Phys. Stat. Sol. (a) 166 (1998).
[11] H. Lichte, Ultramicroscopy 38 (1991) 13.
[12] F. Zemlin, K. Weiss, P. Schiske, W. Kunath, K.-H. Herrmann, Ultramicroscopy 3 (1978) 49.
[13] D. Typke, K. Dierksen, Proc. Autumn School on Image Interpretation and Image Processing in Electron Microscopy, Halle, 1992, 96.
[14] W.O. Saxton, Ultramicroscopy 58 (1995) 239.
[15] A. Thust, 1996, private communications.
[16] A. Thust, M.H.F. Overwijk, W.M.J. Coene, M. Lentzen, Ultramicroscopy 64 (1996) 249.
[17] O.L. Krivanek, P.A. Stadelmann, Ultramicroscopy 60 (1995) 103.